Originally published as:

Priegnitz, M., Thaler, J., Spangenberg, E., Rücker, C., Schicks, J. (2013): A cylindrical electrical resistivity tomography array for three-dimensional monitoring of hydrate formation and dissociation. - *Review of Scientific Instruments*, *84*, 104502

A cylindrical electrical resistivity tomography array for three-dimensional monitoring of hydrate formation and dissociation

Mike Priegnitz,[1,a)] Jan Thaler,[1] Erik Spangenberg,[1] Carsten Rücker,[2] and Judith M. Schicks[1]

[1]*Helmholtz Centre Potsdam, GFZ German Research Centre for Geosciences, Telegrafenberg, Potsdam 14473, Germany*
[2]*Institute of Applied Geosciences, Technical University Berlin, Berlin, Germany*

The LArge Reservoir Simulator (LARS) was developed to investigate various processes during gas hydrate formation and dissociation under simulated *in situ* conditions of relatively high pressure and low temperature (close to natural conditions). To monitor the spatial hydrate distribution during hydrate formation and the mobility of the free gas phase generated during hydrate dissociation, a cylindrical Electrical Resistivity Tomography (ERT) array was implemented into LARS. The ERT contains 375 electrodes, arranged in 25 circular rings featuring 15 electrodes each. The electrodes were attached to a neoprene jacket surrounding the sediment sample. Circular (2D) dipole-dipole measurements are performed which can be extended with additional 3D cross measurements to provide supplemental data. The data quality is satisfactory, with the mean standard deviation due to permanent background noise and data scattering found to be in the order of 2.12%. The measured data are processed using the inversion software tool Boundless Electrical Resistivity Tomography to solve the inverse problem. Here, we use data recorded in LARS to demonstrate the data quality, sensitivity, and spatial resolution that can be obtained with this ERT array. © *2013 AIP Publishing LLC*. [http://dx.doi.org/10.1063/1.4825372]

I. INTRODUCTION

Gas hydrates are naturally occurring crystalline solids formed from water and small gas molecules (< 1 nm). The water molecules build a three-dimensional network of cavities via hydrogen bonds. Those cavities are occupied by "guest" gas molecules. Therefore, gas hydrates belong to a class of compounds known as clathrates or inclusion compounds.[1]

Natural gas hydrates form, as long as all of the following four conditions are fulfilled: (1) elevated pressure, (2) low temperature, (3) presence of sufficient amounts of water, (4) presence of sufficient amounts of gas. Due to the origin of natural gases, most gas hydrates feature methane as guest molecule but higher hydrocarbons and other constituents can be found as well (see, e.g., Sloan and Koh[1]). As the four formation conditions are fulfilled at all active and passive continental margins, deep inland seas, and permafrost areas, gas hydrates exist in quantities large enough to be considered as a potential energy resource.

In the framework of the German national gas hydrate project, SUGAR, the formation and dissociation of methane hydrates within the LArge Reservoir Simulator (LARS) were investigated. Methane hydrate has been formed successfully from methane saturated saline water under simulated *in situ* conditions while temperature and pressure profiles have been recorded. Production tests, using thermal stimulation or pressure reduction for the dissociation of hydrates were successfully performed (e.g., Schicks *et al.*[2,3]). However, there was no way to image the spatial distribution of hydrate crystals during hydrate formation and dissociation, nor could the free methane gas phase released during hydrate dissociation be tracked.

In geophysical aspects, the acoustic velocities and electric properties are more strongly affected by the presence of gas hydrates within some material than other properties.[4] On a laboratory and numerical basis, much work has been previously done to investigate and model both the formation and dissociation of gas hydrates in porous media. Klapproth *et al.*[5] investigated the formation of gas hydrates in gas saturated sediments by transformation of liquid water. They investigated quartz and mixtures of quartz and montmorillonite and kaolinite, respectively. The results show that each mineral play individual interaction with water and gas hydrate. Since the fraction of water was between 10% and 17%, the formed hydrate appears between the quartz grains like cement. Priest *et al.*[6] also interpreted from their measurements of seismic velocities on artificial hydrate-bearing sand samples and cementing effect of hydrates. On the other hand, Spangenberg[7] modelled the electrical resistivity of hydrate-bearing sediments assuming that hydrate forms as a non-cementing material in the pore space. The results of this modelling correspond very well with the experimental results where hydrates were formed from a methane saturated water phase in glass bead sediments.[8] Schicks *et al.*[9] performed experiments under simulated *in situ* conditions in a pressure cell. Under a microscope, they also observed hydrate formation in pore spaces without any contact to sediment grains.

Apparently, the role of formed hydrates differs and the results investigating hydrate formation strongly depend on the technical implementation. However, to mimic naturally

---

a)mikep@gfz-potsdam.de

| **84**, 104502-1 |

occurring marine gas hydrate reservoirs, it seems to be reasonable to assume hydrate formation from the dissolved phase, where hydrates form uniformly distributed without preferred grain contact in the completely fluid saturated pore space.

Hydrate dissociation scenarios within porous media were simulated by Jang and Santamarina[10] with respect to gas recovery and residual gas saturations. Kwon *et al.*[11] modelled the P-T evolution along the phase boundary during hydrate dissociation and the effect of capillarity. They found that pore fluid pressure generation is proportional to the initial hydrate fraction and the sediment bulk stiffness but inversely proportional to the initial gas fraction and the gas solubility.

To better understand the mechanisms affecting hydrates to form and dissociate, tomographic imaging techniques are desirable. However, such tomographical systems to monitor the evolution of gas hydrates within sediments are not yet commonly established. On field scale, tomographical investigations have been done regarding the electromagnetic and seismic properties of hydrate bearing sediments. For example, Weitemeyer *et al.*[12] carried out a controlled source electromagnetic (CSEM) survey to detect gas hydrates at Hydrate Ridge, Oregon, USA. Bauer *et al.*[13] performed cross-well seismic tomography to investigate P-wave velocity, P-wave anisotropy, and P-wave attenuation in hydrate bearing sediments at the Mallik 5L-38 gas hydrate production research well.

On a laboratory scale, Kneafsey *et al.*[14] performed experiments in a pressure vessel on sand samples using X-ray computed tomography (CT) to monitor local density changes during the formation and dissociation of methane hydrates. They observed significant water migration and possible shifting of mineral grains in response to hydrate formation and dissociation, respectively. Since X-ray CT relies on density and the density of water and hydrate is very similar, X-ray CT cannot capture hydrate formation from the dissolved phase. Because this hydrate formation method is essential to mimic nature, suitable laboratory experiments need to be done together with a geophysical monitoring of the evolution of the hydrate content in porous sediment. However, to transform the monitored distribution and evolution of physical properties into the distribution and evolution of hydrate saturation, improved interpretation models are required.

Gas hydrate, like ice, is an electrical insulator. Similarly, hydrate formation, like ice formation, consumes water but excludes dissolved salt ions, meaning the electrical conductivity of the pore fluid increases with increasing hydrate saturation when using brine as a pore fluid. This builds up a high resistivity contrast between the forming hydrate crystals and the remaining fluid within the pore space.

During the hydrate dissociation process, the stationary electrically insulative gas hydrate converts into a mobile, high resistivity free gas phase and liquid water. Therefore, huge differences in the electrical properties within a specimen are expected during both the hydrate formation and dissociation processes, providing a strong signal that can be used for further geoelectrical analyses.

Commonly, multi-electrode geoelectrics are carried out using four electrodes. Two electrodes are used for current injection and two electrodes record the corresponding

potential changes to gain information about the resistivity distribution within the investigated volume. This study presents a multi-electrode system composed of 375 electrodes to perform a cylindrical Electrical Resistivity Tomography (ERT) measurement to investigate the formation and dissociation of gas hydrates on a laboratory scale.

II. EXPERIMENTAL SETUP

In the framework of the SUGAR project, LARS is intended to provide experimental data relevant for testing innovative methods and approaches for producing methane from hydrate-bearing reservoirs. The ERT array was designed to provide an imaging capability while remaining compatible with existing LARS components and experimental conditions. Here, we briefly summarize the LARS system, then describe how the ERT is installed and operated.

A. LARS

To study the evolution of gas hydrates under simulated conditions close to natural conditions, a LARS has been developed (Fig. 1). A key aspect of this system is that hydrate is formed via the circulation of methane saturated water through the sediment. As highlighted in the Introduction, during the hydrate formation process, no free gas phase is present within the pressure vessel. This dissolved-phase hydrate formation technique fills the specimen pore space at rates in the order of 1%−2% per day.

Further details regarding LARS can be found in Schicks *et al.*[2]

Subsequent to the description of Schicks *et al.*,[2] the pressure vessel was modified to include steel mesh-plates and porous filter plates at the fluid in- and outlets of the pressure vessel (Fig. 2). The mesh-plates are directly in front of the inlet and outlet fluid capillaries to homogeneously distribute fluid over the entire cross sectional area of the pressure vessel. The porous filter plates are mounted on the specimen side of the mesh-plates and serve as a mechanically constraining fluid distributor. During both fluid injection and production, no pressure gradients should develop within the porous filter plates, as the fluid flow field only starts to change rapidly in the mesh-plates. Hence, a homogeneous fluid flow field within the sample is created.

Prior experiments considered temperature, pressure, and properties of the pore fluid, specifically the pore fluid's electrical conductivity. Frequent pore fluid sampling transferred the electrical conductivity increase into hydrate formed in LARS considering the salinity increase of the remaining water (Spangenberg and Kulenkampff[15]). This allowed the amount of hydrate formed to be calculated, but did not allow researchers to exactly localize and determine the spatial distribution of hydrate saturations within the sediment sample. Because we have an inhomogeneous temperature field during fluid circulation, hydrate formation rates are assumed to be higher in the colder parts of the sample compared to the warmer regions. To improve the determination of local changes regarding hydrate saturation, an ERT was
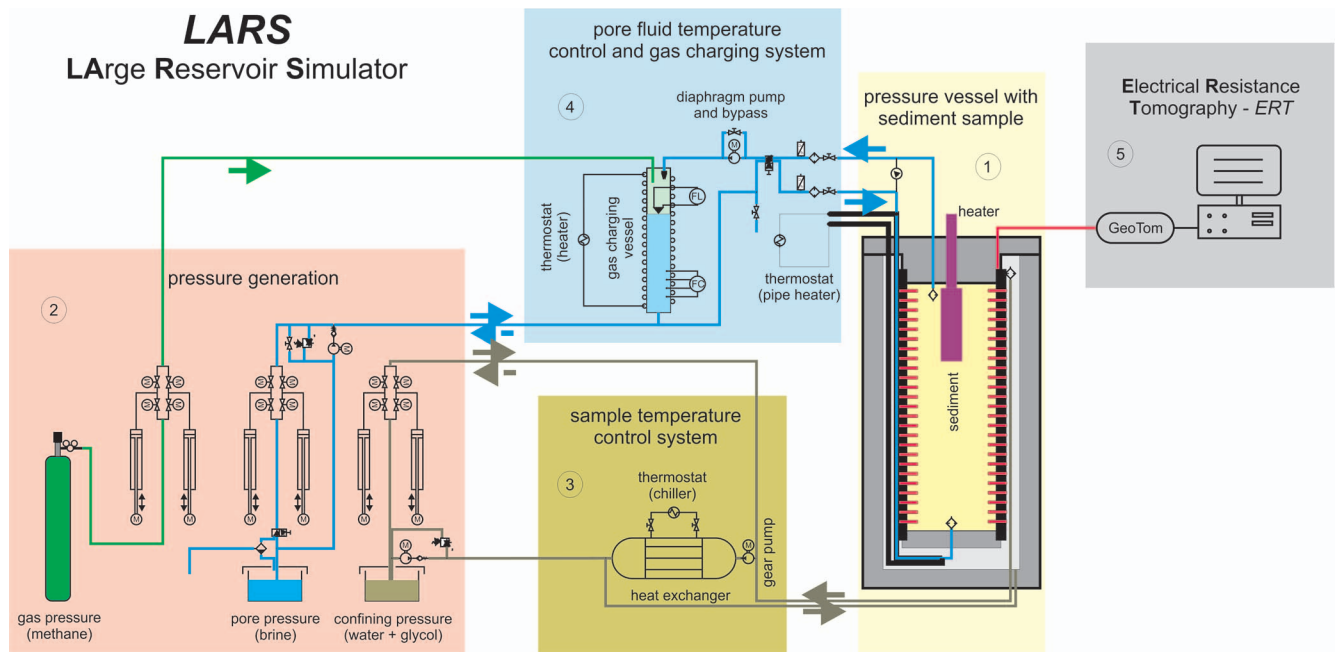
FIG. 1. Schematic of the five major components of LARS: (1) a pressure vessel (volume: 425 l) with a neoprene-jacketed sample and active cooling, (2) a pressure generating system to set up various confining and pore fluid pressure levels, (3) a sample temperature controlling system being able to apply *in situ* temperatures to the sample, (4) a pore fluid temperature control and gas charging system, (5) Electrical Resistivity Tomography (ERT).

implemented into the pressure vessel. The ERT serves as an imaging technique to monitor the spatial distribution of gas hydrates during hydrate formation. During hydrate dissociation, it might be possible to detect features related to gas release, as the produced free gas phase pushes pore fluid out of the pores, possibly increasing the bulk resistivity of the affected regions.

The ERT is attached to the neoprene jacket surrounding the sample material and now constitutes the fifth main component of LARS (5) (see Fig. 1). The ERT array contains 375 electrodes made of stainless steel, each with a sealing PEEK (Polyetheretherketon) casing, attached to the neoprene jacket (marked red in Fig. 1, shown separately in Fig. 3).

All electrodes had to be wired separately through the feed-throughs of the top closure of the pressure vessel of
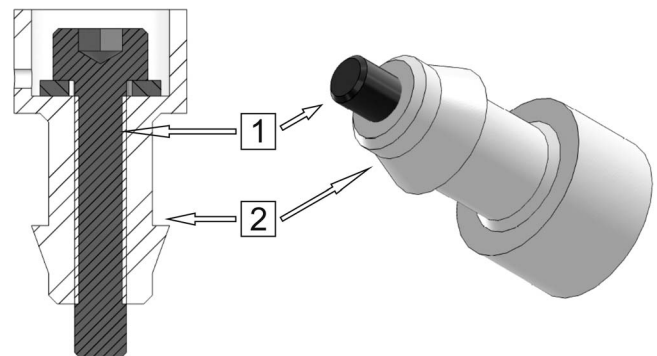

FIG. 3. Technical sketch of the electrodes. (1) Stainless steel M3×16 screw as electrode in (2) a self-sealing PEEK casing. Shown assembly is plugged into the neoprene jacket surrounding the sediment sample.
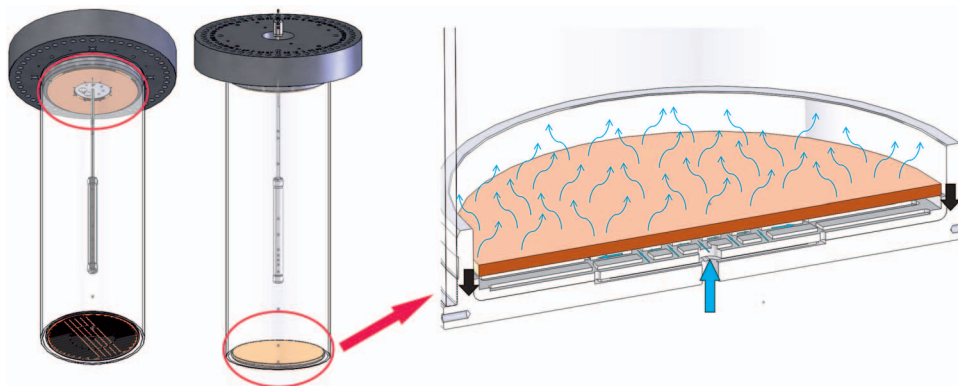

FIG. 2. Location and operation mode of the mesh- (gray) and porous filter plates (orange) in the pressure vessel of LARS.

LARS to provide further linkage to the data acquisition unit.

B. Inversion-boundless electrical resistivity tomography (BERT)

As the mathematical solution of an ERT always involves an inverse problem, the inversion software BERT[16] is used. In short, BERT uses a triple-grid inversion technique that is based on unstructured finite element meshes for forward calculation and parameter identification.[16] By using triangles (2D) and tetrahedrons (3D), BERT can follow arbitrary geometries. BERT is already well described and further details can be found, e.g., in Günther *et al.*[16]

C. Electrode layout

Common cylindrical electrode geometries feature electrode rings producing 2D slices. For multiple rings, the area between two slices gets interpolated during the inversion process. However, determining the optimum number of electrodes composing one ring and the total number of electrode rings is not trivial.

The data acquisition unit (see Sec. II E) limits the maximum number of ERT electrodes to 400. Since we defined to use BERT for data processing, the electrode layout was chosen to optimize the inversion quality in BERT. To find the best combination of the number of rings and the number of electrodes on each ring for 400 electrodes, four synthetic scenarios within LARS with a centred heat source were modelled and inverted:

Scenario I: Initial hydrate formation (increasing resistivity) in the boundary regions

Scenario II: Homogeneous hydrate saturation (high resistivity)

Scenario III: Initial hydrate dissociation at a centred heat source

Scenario IV: Advanced hydrate dissociation around a centred heat source.

Table I presents the inversion results with respect to the number of iterations, the relative root mean square deviation (rrms), and the χ^2 misfit (weighted data functional per data).

Generally, the best inversion results were obtained with the 40×10, 25×15, and 25×16 electrode geometries. Worrying about the mechanical stability of the neoprene jacket, the 40×10 geometry was eliminated. The next best model results were obtained with the 25×15 electrode geometry, and the 375 electrode design with 25 rings featuring 15 electrodes each was chosen (Fig. 4). Choosing 375 electrodes on the outer mantel instead of 400 also provides the future option of placing 25 electrodes at certain positions within the sediment sample.

D. Electrode configuration

Given our chosen electrode geometry, circular 2D slices are measured (Fig. 5(a)). A circular dipole-dipole configuration is chosen for practical reasons, as the required measurement time is $\approx 1/3$ of that required for a Wenner con-

TABLE I. Inversion results for different synthetic LARS scenarios with respect to the electrode geometry (no. of rings × no. electrodes per ring); NaN – Not a Number (not definable, aborted).

	Electrode geometry	No. of iter.	rrms [%]	χ^2
Scenario I	10×40	7	1.95	2.35
	16×25	13	1.13	0.98
	15×25	12	1.08	0.89
	20×20	NaN	NaN	NaN
	25×15	5	0.99	0.89
	25×16	NaN	NaN	NaN
	40×10	5	0.87	0.72
Scenario II	10×40	NaN	NaN	NaN
	16×25	7	2.95	8.71
	15×25	7	2.56	6.53
	20×20	NaN	NaN	NaN
	25×15	11	1.17	1.36
	25×16	6	1.35	1.83
	40×10	5	0.96	0.92
Scenario III	10×40	9	2.74	7.63
	16×25	8	2.60	6.77
	15×25	7	2.66	7.07
	20×20	6	1.79	3.20
	25×15	7	1.21	1.48
	25×16	6	1.33	1.77
	40×10	7	0.87	0.75
Scenario IV	10×40	8	1.63	2.65
	16×25	10	1.10	1.19
	15×25	15	1.00	1.00
	20×20	10	1.02	1.05
	25×15	9	1.02	1.04
	25×16	9	1.00	1.00
	40×10	6	0.99	0.99

figuration, and the penetration depth is much bigger. The measurement utilizes a fixed current injection dipole (electrodes A and B), while the potential measuring dipole (electrodes M and N) is shifted along the circular array (Fig. 5(b)). After six pairings of the M and N electrodes, providing 180° coverage (see Fig. 5(b)), the injection dipole is shifted by one electrode along the circular array and the potential measurements are repeated. This procedure is repeated until the injection dipole has covered 360° of the circular array, resulting in 90 individual measurements per 2D slice. Applying this measurement routine to all 25 circular 2D slices results in a total of 2250 individual measurements.

During data analysis, the volume between the measured 2D slices is inverted with respect to optimal model fitting. Besides the circular 2D dipole-dipole measurements, many other electrode configurations can be added to provide additional information. As the number of different electrode configurations is so large and their choice depends on the focus of investigation, other possible electrode configurations are not discussed at this point.

E. Data acquisition unit

Electrical measurements were performed using the high resolution multi-electrode multi-channel resistivity system
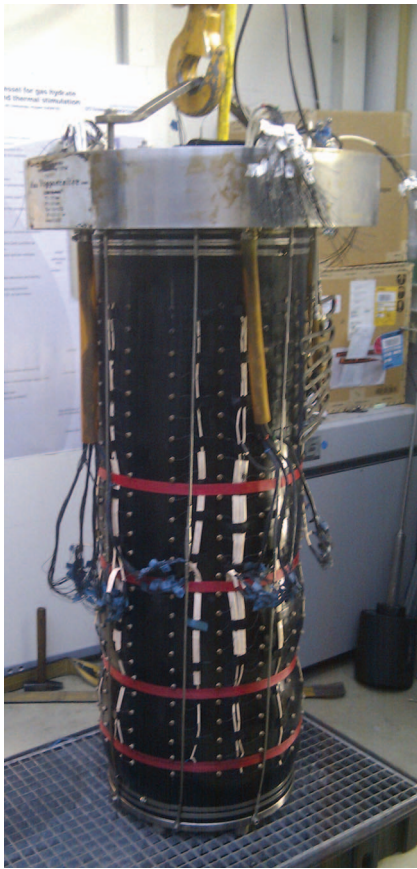
FIG. 4. Photograph of the specimen featuring the finalized 25 × 15 electrode geometry. An overhead crane connects via the yellow hook to the LARS top cap (silver) to support the specimen and lower it into the LARS pressure vessel. The vertical spacing between two neighbouring electrode rings is set to 45 mm and the horizontal spacing between two neighbouring electrodes is set to 100 mm.
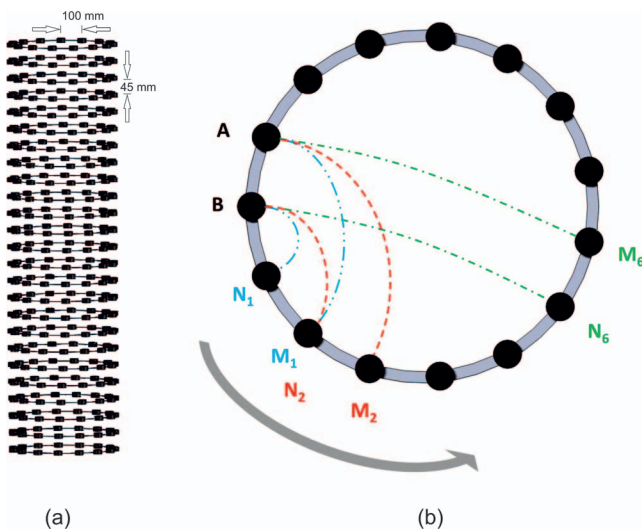

FIG. 5. Scheme of electrode configuration: (a) general electrode geometry with 25 electrode rings featuring 15 electrodes each, (b) circular dipole-dipole configuration with the current injection dipole at electrodes A and B, and the potential measuring dipole at electrodes M and N.

GeoTomMK8E1000 RES/IP/SP by GEOLOG 2000 (Augsburg, Germany). This unit supports a maximum of 400 electrodes and provides measurement resolutions down to 1 μV with an accuracy of 0.5%. Furthermore, frequencies between 1.042 Hz and 25 Hz and input currents from 0.001 mA up to 200 mA can be applied.

Individual electrode sequences can be programmed so that automatically scheduled measurements can be performed.

F. Measurement parameters

Prior to the electrical measurements, parameters such as applied frequency and input current have to be determined.

As no frequency-dependent effects regarding the electrical resistivity are expected for frequencies smaller than 30 kHz (shown by Pearson *et al.*[4] on tetrahydrofuran (THF)-hydrate saturated samples), the measurement frequency was set to the maximum value of 25 Hz to reduce the measurement time as much as possible. A complete measurement run at 25 Hz lasts approximately 35 min. Since the measured pore space hydrate formation rates are in the order of 1%–2% per day, we consider the measurements as steady state during the required measurement time. As mentioned above, the pore water salinity increases with increasing hydrate saturation within the pore space. Hence, the promoting effect of electrolysis at the electrodes for high pore fluid salinities (high hydrate saturation) has to be taken into consideration when choosing the magnitude of the input current. In water, electrolysis leads to the disintegration of water molecules into hydrogen and oxygen. The formation of gas bubbles at the electrodes, distorting the pore fluid properties and thus the ERT measurements, should be avoided. For measurements using a pore fluid with an initial salinity of 2.7 g/l, it has been found that an input current of 10 mA already causes small electrolysis effects at the electrodes for hydrate saturations greater than 70% (corresponding to a pore fluid conductivity of ≈12 mS/cm). Thus, for comparable initial salinities, the input current has to be 1 mA or smaller when high hydrate saturation is desired.

III. DATA QUALITY AND PRELIMINARY RESULTS

A. Data quality: Noise and reproducibility

To quantify the permanent noise effects during the measurements, a very simple scenario has been set up in LARS and measured repeatedly every 6 h for more than six days (26 measurements in total). This scenario utilizes a homogeneous sediment material and a predefined pore fluid of known salinity. The sediment sample was chosen to be medium to coarse quartz sand with a grain size distribution of ≈89% within the interval of 1000–500 μm. The pore fluid is distilled water with 3.68 g/l NaCl, resulting in a pore fluid conductivity of 6.5 mS/cm. The boundary conditions such as surrounding pressure (3 MPa) and temperature were kept constant (20 °C) during the noise measurements, so that no significant changes are expected during the measurements.
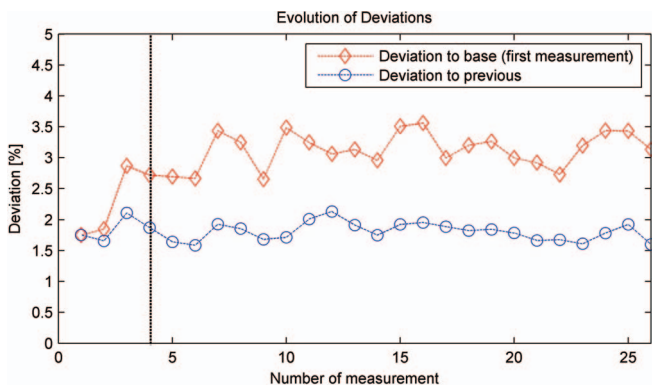
FIG. 6. Evolution of the deviations during the 26 noise measurements (6 h increment), blue line: deviation to the previous measurement, red line: deviation to the first measurement. The vertical dashed line marks the first 24 h it takes the system to reach thermal and chemical equilibrium at given pressure.

The deviation evaluation (Fig. 6) for the noise measurements was estimated as follows: Every measurement run featured 2250 individual dipole-dipole measurements. For the blue line in Fig. 6, each dipole-dipole measurement was compared with its prior value and the deviation was determined. The 2250 deviation values thus obtained were summarized to a mean value and plotted against the measurement number. Hence, the blue line displays the mean deviation of every complete noise measurement to its prior value. The graph appears smooth and free of any trends, only fluctuating around 1.81%.

However, those deviations do not yield any information on the total trend of the deviation. The observed deviations of a noise measurement compared to its previous value could either be caused by a continuous divergence, e.g., in terms of a continuous deviation increase, or by a statistic distribution around a mean value. The red line in Fig. 6 compares the 2250 individual dipole-dipole measurements of all 26 noise measurements with the data from the very first measurement run. This comparison considers the temporal deviation to a base measurement and thus yields information on the total deviation trend. One observes that the red line in Fig. 6 fluctuates around some value between 2.5% and 3.5% and seems to hover around a mean value. This indicates that each dipole-dipole measurement appears to be statistically distributed around a mean value and one can assume the standard deviation for all 2250 individual measurements is caused by permanent background noise. Generally, the most deviation variations are observed within the first 3–4 noise measurements, corresponding to the first 18–24 h. After this period (marked by the vertical dashed line in Fig. 6), the deviations appear much more stable. Hence, it seems like it takes the entire system ≈24 h to reach thermal and chemical equilibrium at given pressure.

Fig. 7 presents the standard deviation of all 2250 individual dipole-dipole measurements made during the 26 noise measurement runs. One observes the standard deviation generally shows satisfactory values. 93.1% of the dipole-dipole measurements display deviations smaller than 5% and 87% of the total data show deviations even smaller than 3%. The mean standard deviation of all 2250 individual dipole-dipole measurements was found to be 2.12%.
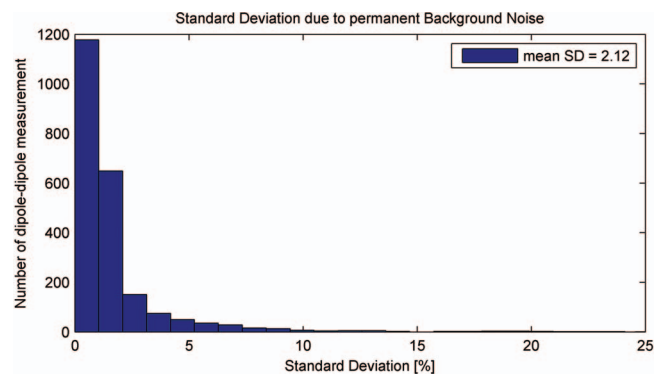

FIG. 7. Standard deviations of all 2250 dipole-dipole measurements determined with the 26 noise measurement runs.

The inverse problem of the data sets is solved during the inversion process. According to the basic equations for geoelectrical investigations formulated by Archie,[17] the electrical resistivity for fully saturated porous materials is given by

$$\rho_s = \frac{a}{\phi^m} \rho_{fl}, \qquad (1)$$

where ρ_s denotes the formation resistivity of the sample material fully saturated by the fluid of resistivity ρ_{fl}, ϕ is the formation porosity, and a and m are empirical parameters. Note, that the inversion process is generally affected by numerous inversion parameters (starting model, regularization, etc.) and the inversion errors and deviations thus have to be considered separately.

As Eq. (1) is composed of constant parameters for a given sample material, the formation resistivity ρ_s is mainly influenced by the resistivity ρ_{fl} of the pore filling material. To estimate the possible influences of the sediment material on the pore fluid, four pore fluid specimens solutions were chemically analysed. Initially, all solutions featured only distilled water and ≈3.6 g of NaCl. One solution has been circulated through the LARS setup for several days, granting long term contact with the quartz sand described above. The remaining three solutions were prepared identically to the first, but separately in the laboratory and analysed without being in contact with the sediment at all. The results of the pore fluid analysis are given in Table II.

The results show the pore fluid composition is strongly influenced by the sediment contact. The ratio of Na to Ca, K, and Mg differs: it turned out that the relative concentration of Ca, K, and Mg increases due to the sediment contact.

TABLE II. Pore fluid analysis, comparison of circulated pore fluid (long term sediment contact) to similar prepared solutions without any sediment contact (three separate attempts to make exactly the fluid circulated through the specimen); values in mg/l.

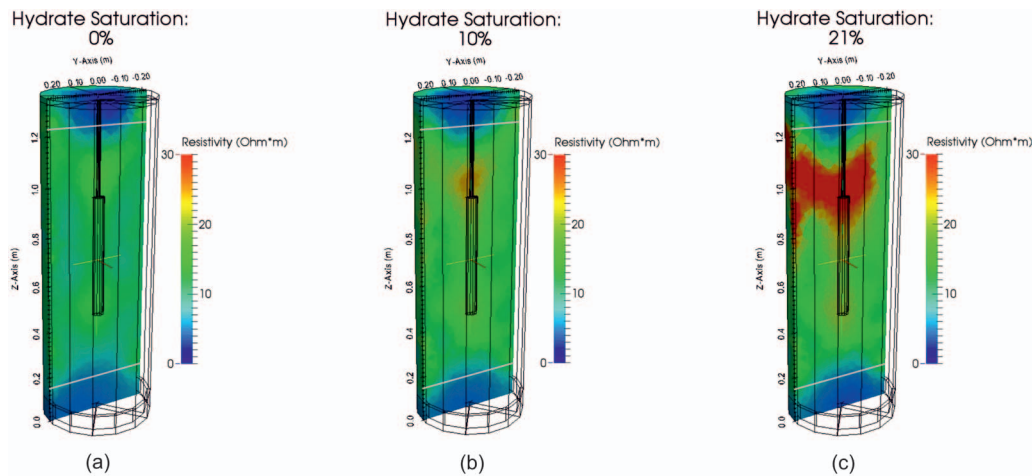|	Na	Ca	K	Mg
Circulated pore fluid	1420	19	<20	2.9
Prepared solution I	1280	3.4	<10	0.64
Prepared solution II	1365	2.2	<10	0.44
Prepared solution III	1233	3.1	<10	0.50

FIG. 8. Inversion results within LARS with a centred heat source for three states of hydrate formation. The horizontal gray lines mark the top and bottom bound of the electrode array. Data beyond these lines constitute an extrapolation of the inversion algorithm. (a) An almost homogeneous resistivity distribution exists at 0% hydrate saturation. (b) For 10% pore space hydrate saturation, no significant changes are observed as the formed hydrates are assumed to be widely spread within the reservoir and the resistivity increases homogeneously by ≈ 2 Ω m. Some localized hydrate formation near the top of the heat source can be seen, however. (c) The first widespread high resistivity accumulation is observed in the top area for 21% hydrate saturation.

This indicates mineral and thus ion exchange during sediment contact with the pore fluid, which may need to be considered depending on the aim of the experiment. However, for the ERT presented here, the ion exchange process does not result in measurable fluid conductivity changes and can be neglected.

B. Preliminary results

The ERT has been applied to a hydrate formation experiment within LARS. The water saturated quartz sand specimen described above was set to P-T-conditions deep in the stability field for methane hydrate (4 °C and 11.5 MPa). The circulating water was sprayed through the gas headspace in the gas-water-interface chamber to dissolve methane in the circulating water. To avoid hydrate formation in the gas-water-interface chamber, it is set to a temperature of 20 °C. The methane charged water enters the sample at a temperature slightly above hydrate stability to avoid clogging the fluid inlet. The water cools down as it migrates through the cold sediment. As the fluid temperature drops, the water cannot hold as much methane in the dissolved phase. Excess methane comes out of solution to form hydrate. As hydrate formation consumes water but excludes the salt ions, repeated electric conductivity measurements of the pore fluid can be used to estimate the actual degree of pore space hydrate saturation (see, e.g., Spangenberg and Kulenkampff[15]). The inversion results (Fig. 8) show the ERT is capable of monitoring the hydrate formation within the specimen.

As the fluid flow direction in this case is from top to bottom, the relative warm pore fluid enters the autoclave from the top. The top and bottom 14.5 cm of the neoprene jacket are not covered by electrodes and hence constitute an extrapolation region during the inversion process. The low resistivity areas at the top and bottom end faces can thus not be considered as actual measured phenomena. Moreover, the extrapola-

tion of both areas is considered to be influenced by insufficient thermal insulation due to wiring and by massive metal influences from the top and bottom closures.

At the beginning of the experiment, the ERT results yield an almost homogeneous resistivity distribution in the order of ≈ 9 Ω m. Assuming Archie's[17] equation with a saturation exponent of 2 (Fig. 9, blue line), or the to date only available measured dependence of resistivity index I on saturation[15] (Fig. 9, black circles)

$$I = \frac{\rho_t}{\rho_0}, \qquad (2)$$

where ρ_t is the true measured resistivity and ρ_0 is the resistivity at 100% water saturation, we cannot expect a strong resistivity increase in the ERT results at low hydrate saturations (see Fig. 9). At a homogeneous hydrate saturation of about 10%, the resistivity is expected to increase by a factor of about 1.2 (see Fig. 9) which matches the data (resistivity increase of ≈ 2 Ω m) very well. The majority of the formed hydrates at this stage can thus be assumed to be widely distributed within the reservoir. Interestingly, the first small block of elevated
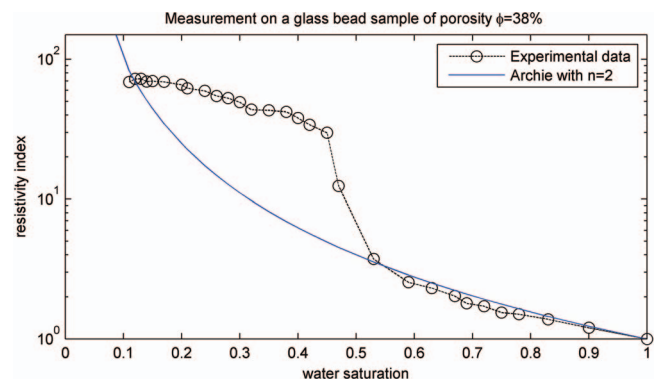

FIG. 9. Measured resistivity index evolution (black circles) versus water saturation compared to Archie's equation with a saturation exponent of 2 (blue line), modified after Spangenberg and Kulenkampff.[15]

resistivity appears to establish in the upper centre at the top of the thermal heat source. This could be either caused by additional nucleation points provided by the thermal heat source or by the enhanced thermal conductivity of the metal heat reactor, carrying the low temperatures fast into the specimen's centre. Since hydrate formation is considered a statistic process, further measurements are required to prove if this phenomenon is random or systematic. However, for hydrate saturations greater than 20%, we see areas in the ERT images where resistivity increased by a factor of about 2. From the small centre block, hydrate formation appears to expand to the boundary regions of the reservoir. The mentioned dependencies (Fig. 9) suggest for such areas local hydrate saturations between 30% and 40%.

Generally, active cooling from the surrounding is assumed to promote hydrate formation especially in the boundary regions, as the stability conditions are first fulfilled where the temperatures are lowest. Therefore, high resistivity methane hydrate accumulations are mainly expected in the boundary regions of the autoclave during the hydrate formation process.

IV. SUMMARY

The cylindrical ERT feature of LARS presented in this study constitutes a remote-sensing method of monitoring the gas hydrate evolution. The 375 electrode system yields satisfying, reproducible data quality, with a mean standard deviation of 2.12%. Measuring the resistivity distribution within the investigated volume can provide new insights into the spatial distribution of forming hydrate crystals.

Unlike X-ray CT, the ERT is capable of monitoring hydrate formation from the dissolved phase. Measurements can be performed under simulated *in situ* conditions, while relatively short measurement times of $\approx$35 min provide adequate time resolution. The spatial sensitivity of the ERT still needs to be quantified, but appears to be in the region of 5–10 cm.

[1]E. Sloan and C. Koh, *Clathrate Hydrates of Natural Gases*, Chemical Industries (CRC Press, 2008).

[2]J. M. Schicks, E. Spangenberg, R. Giese, B. Steinhauer, J. Klump, and M. Luzi, Energies **4**, 151 (2011).

[3]J. M. Schicks, E. Spangenberg, R. Giese, M. Luzi-Helbing, M. Priegnitz, and B. Beeskow-Strauch, Energies **6**, 3002 (2013).

[4]C. Pearson, J. Murphy, and R. Hermes, J. Geophys. Res., [Solid Earth] **91**, 14132, doi:10.1029/JB091iB14p14132 (1986).

[5]A. Klapproth, K. S. Techmer, S. A. Klapp, M. M. Murshed, and W. F. Kuhs, in *Proceedings of the 11th International Conference on the Physics and Chemistry of Ice, Bremerhaven, Germany, 23–28 July 2006* (Royal Society of Chemistry, 311, 2007), p. 321.

[6]J. A. Priest, A. I. Best, and C. R. I. Clayton, J. Geophys. Res., [Solid Earth] **110**, B04102, doi:10.1029/2004JB003259 (2005).

[7]E. Spangenberg, J. Geophys. Res., [Solid Earth] **106**, 6535, doi:10.1029/2000JB900434 (2001).

[8]E. Spangenberg, J. Kulenkampff, R. Naumann, and J. Erzinger, Geophys. Res. Lett. **32**, L24301–L24303, doi:10.1029/2005GL024107 (2005).

[9]J. M. Schicks, M. Luzi, J. Erzinger, and E. Spangenberg, in *Proceedings of the 11th International Conference on the Physics and Chemistry of Ice, Bremerhaven, Germany, 23–28 July 2006* (Royal Society of Chemistry, 311, 2007), p. 537.

[10]J. Jang and J. Santamarina, J. Geophys. Res. **116**, B08202, doi:10.1029/2010JB007841 (2011).

[11]T.-H. Kwon, G.-C. Cho, and J. C. Santamarina, Geochem., Geophys., Geosyst. **9**, Q03019, doi:10.1029/2007GC001920 (2008).

[12]K. A. Weitemeyer, S. Constable, and A. M. Tréhu, Geophys. J. Int. **187**, 45 (2011).

[13]K. Bauer, C. Haberland, R. G. Pratt, F. Hou, B. E. Medioli, and M. Weber, Geol. Surv. Canada, Bull. **585**, 21 (2005).

[14]T. J. Kneafsey, L. Tomutsa, G. J. Moridis, Y. Seol, B. M. Freifeld, C. E. Taylor, and A. Gupta, J. Pet. Sci. Eng. **56**, 108 (2007).

[15]E. Spangenberg and J. Kulenkampff, Geophys. Res. Lett. **33**, L24315, doi:10.1029/2006GL028188 (2006).

[16]T. Günther, C. Rücker, and K. Spitzer, Geophys. J. Int. **166**, 506 (2006).

[17]G. E. Archie, Trans. AIME **146**, 54 (1942).